Fluorinated Mn_3O_4 nanospheres for lithium-ion batteries: Low-cost synthesis with enhanced capacity, cyclability and charge-transport

Nithyadharseni Palaniyandy[a, *]

NPalaniyandy@csir.co.za

Funeka P. Nkosi[a, b]

Kumar Raju[a]

Kenneth I. Ozoemena[b, **]

Kenneth.ozoemena@wits.ac.za

[a]Materials Science & Manufacturing, Council for Scientific & Industrial Research (CSIR), Pretoria 0001, South Africa

[b]Molecular Sciences Institute, School of Chemistry, University of the Witwatersrand, Johannesburg 2050, South Africa

*Corresponding author.

**Corresponding author.

Abstract

A facile synthesis of fluorinated Mn_3O_4 nano-spheres (F-Mn_3O_4) from low-cost electrolytic manganese dioxide (EMD) at different temperatures and times has been reported. While the as-prepared materials are micron-sized (>200 nm) and the fluorinated Mn_3O_4 are nano-sized particles (<50 nm). Detailed characterisation (using XRD, XPS, FESEM and EDX, electrochemistry including EIS) clearly prove the unique effects of the fluorination on the physico-electrochemical properties of the F-Mn_3O_4 nanomaterials, notably the dramatic transition from microstructure to nanostructure. The electrochemical performance of F-Mn_3O_4 is strongly enhanced by the fluorination with high specific capacity (931 mAh g^{-1} at 100 mA g^{-1}), excellent capacity retention (87% after 100 cycles) and excellent rate capability (460 and 216 mAh g^{-1} at 1000 and 2000 mA g^{-1}, respectively) compared to the pristine Mn_3O_4 materials with 556 mAh g^{-1} with the capacity retention of 73%. The performance of the F-Mn_3O_4, which is better or comparable with corresponding materials in the literature, gives exciting promise for potential development of high-performance low-cost manganese oxide-based anode materials for lithium-ion batteries. It is common knowledge in the battery research community that spherical particles are most preferred for industrial application due to improved packing density. Importantly, EIS data provide critical insight into the charge-transfer properties of the anode materials as a result of the fluorination process. The enhanced performance of the F-Mn_3O_4 is attributed to its nano-spherical morphology that favours good fluidity of particles and excellent tap density of the redox-active components.

Keywords: Electrolytic manganese dioxide (EMD); Fluorinated Mn_3O_4 nano-spheres; Anode materials; Lithium-ion batteries; Charge transport

1 Introduction

Lithium-ion batteries (LIBs) dominate the energy storage markets for application in mobile phones, laptops, portable electronics and electric vehicles due to their advantageous properties such as high energy and power densities and long cycle life. The first introduced most common anode materials was carbon. However, anode materials of carbon and its derivatives of graphene show low specific capacity of 372 mAh g^{-1}. In order to enhance the specific capacity of lithium-ion batteries, various anode materials have been proposed such as Si, Sn, Sb and transition metal oxides (Fe_3O_4, CoO, NiO and Mn_xO_y) [1–13] due to their high theoretical capacities that are two to three times greater than carbon. Of the transition metal oxides, manganese oxide materials (Mn_3O_4) have become more attractive due to their special features of high specific capacity, low discharge-charge potential during cycling, low cost and eco-friendliness. However, the Mn_3O_4 materials show some challenges that hinder them from practical applications in LIBs; poor electrical conductivity and volume change during cycling which causes severe aggregation of the particles with the possibility of aggravating the mechanical stability of the electrode materials [14–16]. To curb these problems, three key strategies are being explored by various researchers across the globe. First strategy involves the exploration of nanostructures with different morphologies such as nano-rods [10,17–19], nano-wires [20], nanotubes [21], nano-flowers [22], hollow-spheres [23–25] and nanocrystals [26,27]. However, some of these nano-materials have been found to exhibit poor cycling stability and rate capability. The second strategy involves the use of composite materials (i.e., integrating Mn_3O_4 with some electrically-conducting matrices) such as graphene sheets [28–34], amorphous carbon [35–37] and carbon nanotubes [26]. On the other hand, the third and the most promising strategy for practical application involves doping the Mn_3O_4 with some foreign cations such as Fe-doped Mn_3O_4 [38] or anions

such as N-doped graphene/Mn_3O_4 [19], and F-doped Mn_3O_4 [39]. Fluorine is an important doping agent to yield a high electrical conductivity, enhanced the thermal stability and can act as a good corrosion resistant [40,41].

Despite the importance of F-doping on electrode materials for advanced batteries, there is little knowledge about F-doped Mn_3O_4. In fact, to our knowledge, there is just a single report on F-doped Mn_3O_4 anode material for LIBs [39]. In that study, however, the authors reported the use of manganese acetate (an expensive manganese oxide precursor) in a molten salt strategy (involving extra two inorganic salts) with NaF to generate F-doped Mn_3O_4 with nanowire/nanobelt morphology. In this work, we introduce a simple synthesis strategy involving a high-temperature heating process in a furnace of a very low-cost precursor material, electrolytic manganese dioxide (EMD), to synthesis pure Mn_3O_4 and F-doped Mn_3O_4. Because, fluorine is a significant synergistic doping agent to yield a high electrical conductivity, enhanced the thermal stability and can act as a good corrosion resistant. In this scenario, we have been anticipating that F anion doping can improve the conductivity of Mn_3O_4 material and also enhance the electrochemical performance of the Mn_3O_4 material. In addition, we clearly show how our synthesis strategy is able to generate more industrially-preferred spherical particle morphology with improved physico-electrochemical properties for LIB application (high capacity, excellent rate capability and excellent charge-transport properties).

2 Experimental section

2.1 Preparation of Mn_3O_4 and F-doped Mn_3O_4

Mn_3O_4 samples were prepared by heating raw electrolytic manganese dioxide sample (EMD, 92.46% dry MnO_2, generously supplied by Delta EMD (Pty) Ltd, South Africa) [42] at 850 °C for 22h and 1000 °C for 40 h at the heating/cooling rate of 10 °C/min. The two samples are abbreviated herein as Mn_3O_4-850 °C/22h and as Mn_3O_4-1000 °C/40h, respectively. From the literature [43] the MnO_2 has been prepared by hydrothermal method followed by heating at 350 °C and 500 °C for 10h in air. Also to obtain Mn_3O_4, the material was annealed further by 280 °C and 700 °C for 5h under Ar. Respect to this condition, in the present manuscript, the EMD was directly heated for the two different temperatures (850 °C for 22h and 1000 °C for 40h) to obtain Mn_3O_4 with different morphologies. But all the materials were heated at ambient atmosphere. For fluorination, appropriate amount of NH_4F salt (Sigma Aldrich, > 99.99% purity, 0.3 g, i.e., ~17% of the total weight of material) was dispersed in distilled water and then Mn_3O_4 (1.5 g) was added, stirred with a magnetic stirrer for 5h at room temperature, and then slowly dried at 80 °C overnight (12 h) [44]. Each of the resultant dry powder samples was subjected to thermal treatment at 450 °C for 5h under Ar atmosphere at the rate of 3 °C/mins. The final products are named herein as F-Mn_3O_4-850 °C/22h and F-Mn_3O_4-1000 °C/40h, respectively.

2.2 Characterisation techniques

The prepared samples were evaluated by X-Ray Diffraction (XRD) using PANalytical X'Pert PRO powder X-Ray Diffractometer with a monochromatized Cu Kα radiation of λ = 1.5406 Å at the 2θ range of 10°-90°and the lattice parameters derived by using Rietveld refinement via TOPAS (3). The surface analysis and chemical composition of the compounds have been performed by X-ray photoelectron spectroscopy (XPS) with K-Alpha$^+$ XPS spectrometer using monochromatic Al Kα (1486.6 eV) X-ray source. The binding energy (BE) scale was calibrated by measuring the reference peak of C1s (BE = 284.6 eV). The morphology, EDX and mapping of the materials were analysed by Field Emission Scanning Electron Microscopy (FE-SEM) carried out using JEOL JSM-7500F. Transmission electron microscopy (TEM) was obtained from JEOL-JEM 2100, operated at an acceleration voltage of 200 kV. The electrode fabrication was carried out by mixing together the active material (Mn_3O_4 or F-Mn_3O_4), polyvinylidene fluoride (PVDF-MTI corporation) as a polymer binder and Super-P carbon black in 70: 15: 15 wt%, respectively in N-methyl-pyrrolidinone (NMP > 99.5% purity, Gelon LIB) solvent. The mixed slurry was kept overnight (12 h) for proper mixing under magnetic stirrer. The slurry was coated on Cu (Gelon LIB) foil by using Doctor Blade Technique (DBT) and then the foil was cut into circular shape of 16 mm in diameter. The geometrical electrode area was *ca.* 2 cm^2 and mass of active material was 3–4 mg. The Coin Cells were then assembled in an Ar-filled glove box (MBraun MB 150B-G, Germany - maintaining the concentrations of O_2 and H_2O < 1 ppm) by using the fabricated electrodes as an anode, Li metal (Hohsen Corp. Japan) as counter electrode and 1 M $LiPF_6$ in ethylene carbonate (EC), diethylene carbonate (DEC) and dimethyl carbonate (DMC) (1: 1: 1 by volume, Merck) as the electrolyte. The fabricated cells were electrochemically characterized by galvanostatic cycling (GC) using MACCOR series 4000 tester. Cyclic voltammetry (CV) and electrochemical impedance spectroscopy (EIS) was evaluated by using a Bio-Logic VMP3 potentiostat/galvanostat controlled by EC-Lab v10.40 software at the scan rate of 0.1 mV s^{-1} with the potential range of 0.005–3.0 V. The EIS plots were recorded by applying 10 mV amplitude over the frequency range from 100 kHz to 10 mHz at room temperature and the data was analysed by using Z-view software (version 2.2, Scribner Assoc. Inc. USA), respectively.

3 Results and discussion

The XRD patterns of the F-doped and un-doped samples (Fig. 1a) clearly exhibit tetragonal structure (hausmannite-Mn_3O_4) with space group $I4_1/amd$, corresponding JCPDS card: # 24-0734 (a = 5.765 and c = 9.472 Å). Compared to un-doped Mn_3O_4, there is a peak shift observed in both F-doped samples, which clearly indicates the Mn_3O_4 was successfully doped with fluorine. With the exception of peak (103) of the F-doped Mn_3O_4 that showed a very slight positive shift (~0.7° shift), all the peaks essentially occur at the same positions (see Fig. 1 and Fig. S1). The slight changes in the (103) peak is due to the weakly distorted octahedral sites [MnO_6] in which the O_2^- (ionic radius 0.132 nm) are replaced by F^- (ionic radius 0.133 nm) [45]. The negligible change in the lattice parameter of the F-doped materials may be related to the negligible difference in the ionic radii of oxygen and fluorine. Also, there is a small peak at 55.2° may be due to impurity of the fluorinated samples. Fig. 1 (b, c) exemplifies the Rietveld refinement for Mn_3O_4-850 °C/22h and F-Mn_3O_4 -850 °C/22h, which is in very good agreement with JCPDS pattern and literature. The crystallite size and the lattice parameters were calculated from TOPAS and are given in Table 1. The crystallite size of Mn_3O_4 decreased upon fluorination (F-Mn_3O_4), which is consistent with the XRD peaks (Fig. S1),

showed higher FWHM than the pure Mn_3O_4 material. No other characteristic peaks are detected in the entire XRD pattern.

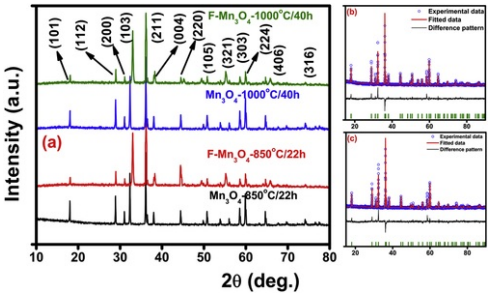

Fig. 1 XRD pattern for all the samples (a), Rietveld refinement XRD pattern of Mn_3O_4- 850 °C/22h (b) and F-Mn_3O_4 -850 °C/22h (c).

alt-text: Fig. 1

Table 1 Lattice parameter and crystallite sizes of the as-prepared Mn_3O_4samples and their fluorinated counterparts.

alt-text: Table 1

Material	Lattice parameter	Crystallite size (nm)
	a (Å) c (Å)	
Mn_3O_4-850 °C/22h	5.761 9.461	91
F-Mn_3O_4-850 °C/22h	5.756 9.460	23
Mn_3O_4-1000 °C/40h	5.759 9.458	121
F-Mn_3O_4-1000 °C/40h	5.753 9.457	19

X-ray photoelectron spectroscopy (XPS) was carried out to further examine the fluorine-doping into the Mn_3O_4, Mn 2p states of F-doped and un-doped materials are shown in Fig. 2 (a, b). Both F-doped samples displayed slight peak shift in the higher energy levels in Mn2p (2p $_{3/2}$ and 2p $_{1/2}$) state than un-doped Mn_3O_4-800 °C/22h and Mn_3O_4-1000 °C/40h, suggesting that some of the oxygen ~~have~~ has been replaced by F^- ions in the Mn_3O_4 material.

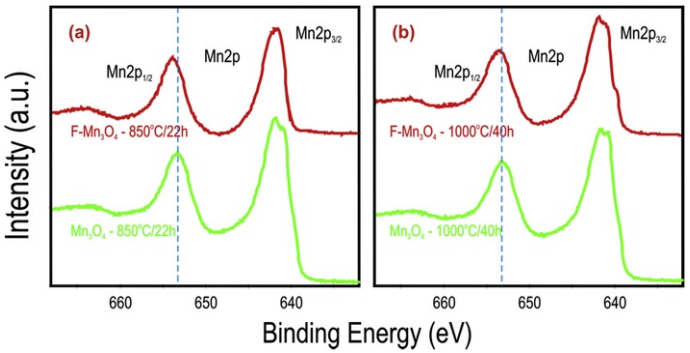

Fig. 2 XPS peaks (Mn 2p) of the F-doped and un-doped Mn_3O_4 samples at 850 °C/22h (a) and 1000 °C/40h (b).

alt-text: Fig. 2

The binding energies and the calculated distance of the materials (Table 2) are in good agreement with literature [4,19,23]. The difference in the XPS data between F1s and O1s is necessary for a conclusive evidence of oxygen replacement by Fluorine. We observed from the O1s spectra (Fig. 3a-d) that the un-doped samples showed peak at 531.5 eV while F-doped materials showed a slight negative shift to around 531 eV. Also, the presence of fluorine is

confirmed from the XPS data wherein the F-doped Mn_3O_4 showed well-defined F 1s peaks at 681 eV (Fig. 3e and f) which is in good agreement with the literature [39]. As shown in Fig. 3e and f, the well-defined F 1s peaks were only observed in the NH_4F-modified Mn_3O_4 material but not in the pristine ones, confirming that some F^- ions have been integrated into the surface lattice of the Mn_3O_4 particle materials.

Table 2 Binding energies of Mn2p and the doublet splitting energy of pure and fluorine doped Mn_3O_4 samples.

alt-text: Table 2

Sample	Mn 2p (eV)		Spin energy gap (eV)
	$2p_{3/2}$	$2p_{1/2}$	
Mn_3O_4-850 °C/22h	642.1	653.4	11.3
Mn_3O_4-1000 °C/40h	641.8	653.1	11.3
F- Mn_3O_4-850 °C/22h	641.9	653.7	11.8
F-Mn_3O_4-1000 °C/40h	641.7	653.5	11.8

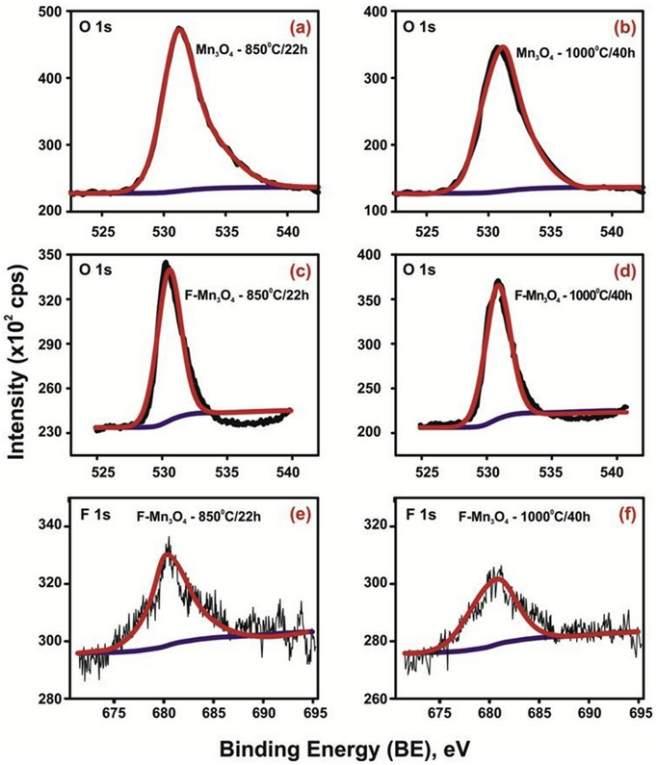

Fig. 3 (a-f) XPS spectra of O 1s and F 1s states of the pristine and 17 wt% NH_4F-modified Mn_3O_4-850 °C/22h, and 1000 °C/40h samples.

alt-text: Fig. 3

Indeed, from the XRD and XPS data, it can be concluded that fluorination of the Mn_3O_4 material was successfully carried out. The chemistry of this fluorination process ~~in~~ may be related to the decomposition of the NH_4F to the NH_3 and HF in a humid condition (i.e., creation of an acidic environment), which allows for an anion-exchange reaction between F^- and O^{2-} ions thereby creating oxygen-ion vacancies at the particle surface. At the high temperature

used in this work, it is expected that the NH_3 and H^+ ions from the acidic HF will be liberated from the lattice, further creating surface defects.

The morphological effects of the un-doped and F-doped Mn_3O_4 samples were evaluated using Field emission scanning electron microscopy (FE-SEM) as shown in Fig. 4a-d. The morphology of Mn_3O_4-850 °C/22h (Fig. 4a) and Mn_3O_4-1000 °C/40h (Fig. 4c) demonstrates the crystalline nature of the particles. The as-prepared material gave an oval/microsphere-like morphology (≥200 nm diameter), while the F-doped samples gave a sphere-like morphology (*ca.* 50 nm diameter). This dramatic change in micron-sized morphology to nano-sized spheres upon doping with fluorine is a clear indication of the effect of the successful fluorination process. The mechanism for this interesting transformation is not fully understood at this time, but suffice it to say that fluorination process inhibits nucleation process but, together with heating, encourages segregation of particle to the nano-spherical particulate sizes (i.e., top-down nanostructuring). The nano-spherical particles are uniformly-distributed and linked with one another in chain-like formation. It is well known in the battery research community that spherical particles are the most suitable or preferred for industrial application due to their improved packing density. That allows for good fluidity of particles, excellent tap density and homogeneous distribution of the redox-active transition metal, Fe and Mn. The changes arising from the fluorination may be associated with similar reasons previously propounded by Jin et al. [39]: the ability of fluorine to co-ordinate with manganese cations and partially replace oxygen atoms, and act as a capping agent, thus influencing the materials strong adsorption on the surface. Clearly indicate the effect of the F-doping, corroborating the XRD, XPS and SEM results. TEM images of Mn_3O_4-850 °C/22h, F-Mn_3O_4-850 °C/22h and F-Mn_3O_4-1000 °C/40h samples are shown in Fig. 5(a-d). Mn_3O_4- 850 °C/22h contains spherical and oval shaped particles in the range of sub-micron size, F-Mn_3O_4-850 °C/22h and F-Mn_3O_4-1000 °C/40h display spherical and nano-sized particles. The dark spots in Fig. 5c, d might be due to the overlapping of particles. In addition, the EDX spectra and mapping images, exemplified of F-Mn_3O_4-850 °C/22h (Fig. 6). In the images, the fluorine was randomly distributed while the other elements were uniformly distributed in the samples. From the EDX spectrum, the estimated atomic ratio of Mn:O is 1: 30.45, while for the F-Mn_3O_4 the ratio of Mn:O:F is 1: 24.63: 0.41.

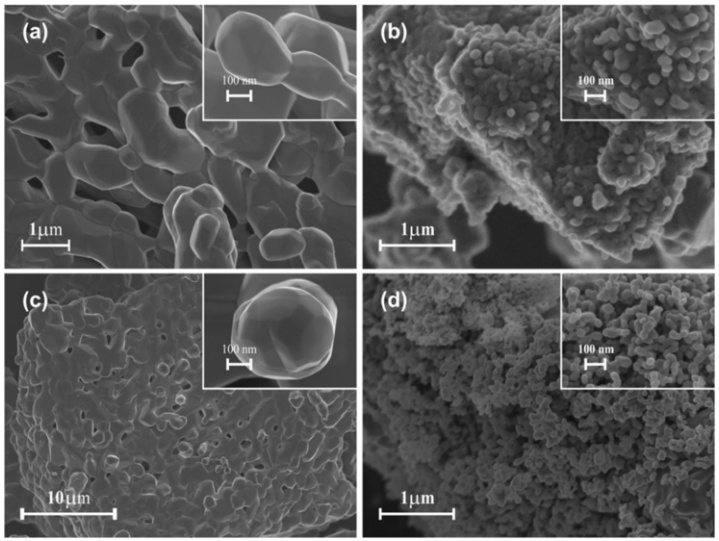

Fig. 4 (a-d) FE-SEM images of pure and doped samples. (a) Mn_3O_4-850 °C/22h, (b) F-Mn_3O_4-850 °C/22h, (c) Mn_3O_4-1000 °C/40h and (d)F-Mn_3O_4-1000 °C/40h

alt-text: Fig. 4

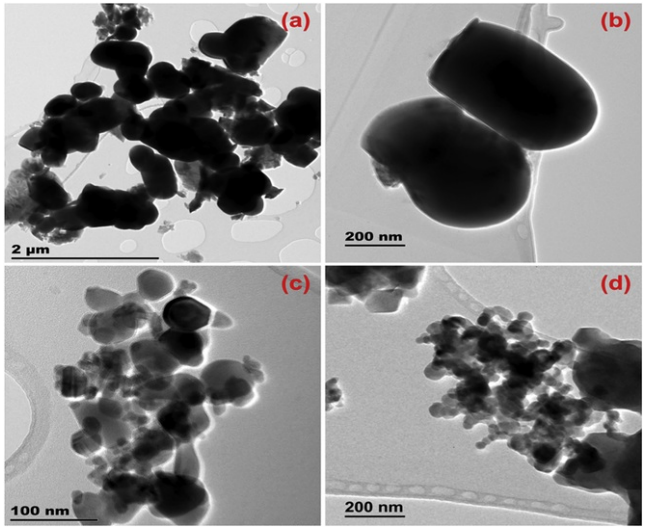

Fig. 5 TEM images of Mn_3O_4-850 °C/22h (a, b) high and low magnifications, F-Mn_3O_4- 850 °C/22h (c) and F-Mn_3O_4-1000 °C/40h (d).

alt-text: Fig. 5

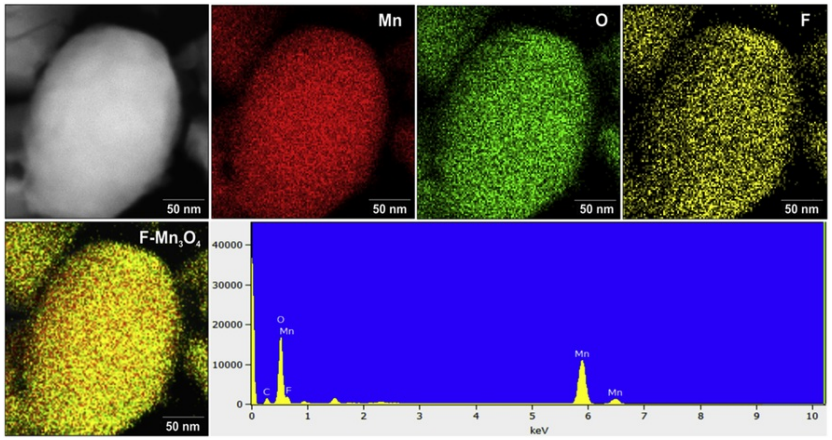

Fig. 6 Typical EDX and mapping images of F-Mn_3O_4-850 °C/22h

alt-text: Fig. 6

The CV curves of pure and F-doped Mn_3O_4 prepared at 850 °C/22h and 1000 °C/40h are shown in Fig. 7(a-d). In the first cycle of all the compounds (pure and F-doped), the cathodic peak at about ~0.6 V vs Li/Li^+ corresponds to the decomposition of the electrolyte which causes the SEI film formation on the electrode surface [19,46,47]. However, the SEI formation peak current area is slightly smaller in the F-doped samples compared to un-doped samples.

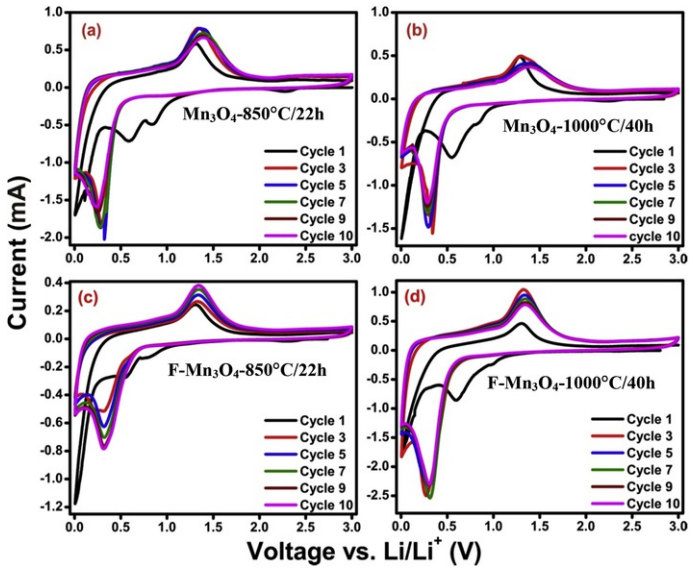

Fig. 7 (a-d) CV curves of ~~P~~pure and doped Mn_3O_4 materials. (a) Mn_3O_4-850 °C/22h, (b) Mn_3O_4-1000 °C/40h, (c) F-Mn_3O_4-850 °C/22h and (d) F-Mn_3O_4-1000 °C/40h, at the scan rate of 0.1 mV s^{-1}, with the potential window of 0.005–3.0 V.

alt-text: Fig. 7

The thorny cathodic peak below at 0.2 V vs Li/Li^+ represent the reduction of manganese oxide [19,46]. After the first cycle, the peak at 0.6 V vs Li/Li^+ disappear and the spiky peak shifts to ~0.35 V vs Li/Li^+, suggesting that the SEI formation and the structural changes during the lithium-ion insertion process only take place during the first cycle. While the strong anodic peak at about 1.3 V vs Li/Li^+ observed in all the samples is due to the oxidation reaction of the metallic manganese to manganese ion. The conversion reaction mechanism for Mn_3O_4 material during lithiation and de-lithiation process can be followed by the equations [19,24,39,48,49].

$$8Li^+ + Mn_3O_4 + 8e^- \leftrightarrow 3Mn(0) + 4Li_2O \quad \textbf{(1)}$$

The integrated area of the peak current for the F-Mn_3O_4-850 °C/22h (Fig. 7c) increases with increasing cycles, but then stabilizing at the 9th cycle. On the other hand, the area of the peak current for the F-Mn_3O_4-1000 °C/40h sample (Fig. 7d) did not show a significant change from the 2nd to the 10th cycle. In contrast, the area of the peak current for the un-doped samples (Fig. 7a and b) decreases with increasing cycle number, signifying capacity fading. The results of the CV evolutions indicate that the F-doped samples give high specific capacity and good cycling properties compared to the un-doped samples.

Next, we subjected the four samples to galvanostatic discharge-charge cycling at a current density of 100 mA g^{-1} with the potential window of 0.005–3.0 V (Fig. 8a and b)~~.~~. First discharge profiles of Mn_3O_4-850 °C/22h (Fig. 8a(i)), F-Mn_3O_4-850 °C/22h (Fig. 8a(ii)), Mn_3O_4-1000 °C/40h (Fig. 8a(iii)) and F-Mn_3O_4-1000 °C/40h (Fig. 8a(iv)) show a sloping voltage in the range from 1.2 to 0.35 V vs Li/Li^+ corresponding to the formation of solid electrolyte interphase (SEI) film and the reduction process of the lithium to manganese oxide [15,19,23,31]. The wide plateau at ~0.35 V Li/Li^+ is due to further reduction of the MnO to Mn; the plateau for the F-doped samples are much wider than those of the un-doped samples, which is a further indication of the unique effect of the fluorination process. However, the nominal voltage of F-doped (*ca.* 0.73 and 0.78 V vs Li/Li^+ for F-Mn_3O_4-850 °C/22h and F-Mn_3O_4-1000 °C/40h) is lower than the un-doped samples (*ca.* 0.9 and 0.8 V vs Li/Li^+ for Mn_3O_4-850 °C/22h and Mn_3O_4-1000 °C/40h) ~~at~~in the first cycle.

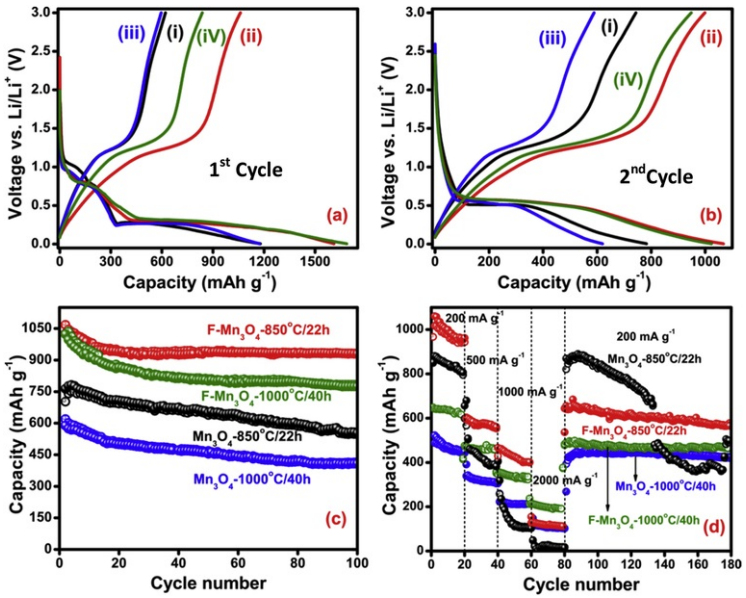

Fig. 8 First (a) and second (b) discharge-charge cycles of Mn_3O_4-850 °C/22h (i), F-Mn_3O_4-850 °C/22h (ii), Mn_3O_4-1000 °C/40h (iii) and F-Mn_3O_4-1000 °C/40h (iv), (c) cycling performance of all the compounds and (d) Rate performance of all the materials cycled with different current densities of 200, 500, 1000 and 2000 mA g^{-1} at the potential window of 0.005–3.0 V.

alt-text: Fig. 8

The first charge profile of all the samples shows a voltage plateau at 1.3 V vs Li/Li^+, could be associated with the oxidation reactions of Mn to Mn_3O_4. The overall first discharge capacities of the compounds were 1179, 1174 and 1610, 1686 mAh g^{-1} for un-doped and F-doped samples, which is almost 1.2 to 1.6 times greater than the theoretical capacity of Mn_3O_4 (937 mAh g^{-1}). The high capacity is related to the conversion process of Mn, Li_2O formation and SEI film formation [23,31]. However, all the materials are suffered from the initial irreversible capacity loss (ICL) (i.e. 397 for Mn_3O_4-850 °C/22h, 554 for Mn_3O_4-1000 °C/40h, 542 for F-Mn_3O_4-850 °C/22h and 663 for F-Mn_3O_4-1000 °C/40h) which may be related to incomplete conversion reaction and the formation of the SEI layer. In the following (2nd) discharge cycle of all the samples (Fig. 8 b), the peak at 0.35 V is shifted to 0.5 V vs Li/Li^+, while the same plateau at.1.2 V vs Li/Li^+ are observed in the charge cycle, however, the same nominal voltage of *ca.*0.6V vs Li/Li^+ was observed for pure and fluorine doped Mn_3O_4 samples. The respective 2nd cycle specific capacity of pure and F-Mn_3O_4-850 °C/22h and F-Mn_3O_4-1000 °C/40h samples are 782, 620 and 1068, 1023 mAh g^{-1}, with the corresponding coulombic efficiencies between ~86 and 90%.

The cycling performances of pure and F-Mn_3O_4 samples are shown in Fig. 8 (c). The pure Mn_3O_4-850 °C/22h showed gradual capacity fading from the initial cycle until the end of the 100th cycles, while Mn_3O_4-1000 °C/40h showed continuous fading up to 80th cycle (420 mAh g^{-1}), then started preserving almost the same capacity until the end of the 100th cycle (416 mAh g^{-1}), but its specific capacity was lower than Mn_3O_4-850 °C/22h (553 mAh g^{-1}). The superior electrochemical properties of Mn_3O_4-850 °C/22h over its counterpart (Mn_3O_4-1000 °C/40h) may be related to its crystalline morphology and the particles arrangement in the system (more uniform spherical morphology) which allows for the enhancement of lithium-ion storage performance. However, both pure materials experience high capacity fading and low capacity, consistent with CV data. The F-Mn_3O_4-850 °C/22h and F-Mn_3O_4-1000 °C/40h reveal high specific capacity with good cycling stability, compared to the pure samples. In the beginning cycles of both samples, the capacity faded gradually and then started maintaining the cycling stability and the capacity, which is in good agreement with the CV data. The overall specific capacity at 100th cycle of Mn_3O_4-850 °C/22h, Mn_3O_4-1000 °C/40h, F-Mn_3O_4-850 °C/22h and F-Mn_3O_4-1000 °C/40h was 553, 416 and 990, 783 mAh g^{-1}, with respective capacity retention of 73, 67, 87 and 77%, respectively. The coulombic efficiency of all the compounds is given in Fig. S2 which is around 90% till first very few cycles and upon cycling the coulombic efficiency was around 99%. The comparison results of our materials with the reported literature conducted at 100 cycles are given in Table 3.

Table 3 Comparing the electrochemical cycling performance of our materials with the available literature.

alt-text: Table 3

Mn_3O_4 material	Reversible capacity (mAh g^{-1})	Current rate (mA g^{-1})	Capacity retention	ref

	1st cycle	after aging			
Mn_3O_4@C nanorod by solvo-thermal reaction	1246	473 after 50 cycles	40	68	[10]
Sponge-like Mn_3O_4 by simple precipitation	1327	800 after 40 cycles	117	92	[15]
Order aligned Mn_3O_4 by electrochemical route	919	882 after 85 cycles	936	96	[16]
Mn_3O_4@TiO_2 by hydrogeneration	~1300	392 after 100 cycles	500	~85	[18]
Mn_3O_4@H-TiO_2 by hydrogeneration	~1210	615 after 100 cycles	500	~100	[18]
Mesoporous Mn_3O_4 nanotube by hydrogen reduction	~920	641 after 100 cycles	500	~91	[21]
Mn_3O_4/Fe_3O_4 nano-flowers by etching	1625	600 after 50 cycles	100	55	[22]
Mn_3O_4 hollow spheres by aerosol based droplet to particle	1609	~980 after 140 cycles	200	~89	[24]
Mn_3O_4/MWCNT nanocrystals by solvo-thermal reaction	1380	592 after 50 cycles	100	63	[26]
Mn_3O_4/GO by co-precipitation	949	792 after 50 cycles	100	83.5	[28]
$Mn_3O_4$by microwave hydrothermal	1300	496 after 50 cycles	40	58	[30]
Mn_3O_4/GS by microwave hydrothermal	1354	900 after 50 cycles	40	~100	[30]
Mn_3O_4 ordered mesoporous carbon by carbonization	1843	802 after 50 cycles	100	90	[35]
Nitrogen-Graphene doped Mn_3O_4 by hydrothermal method	1275	800 after 40 cycles	200	89	[19]
Mn_3O_4@F by molten salt method	1221	615 after 100 cycles	100	75	[39]
Mn_3O_4/RGO by refluxing	1005	553 after 50 cycles	120	80	[48]
Mn_3O_4/GNS by in-situ transformation in an aqueous	1600	500 after 40th cycles	60	72	[49]
Mn_3O_4 -850 °C/22h	1179	553 after 100 cycles	100	73	This work
F-Mn_3O_4-850 °C/22h	1610	990 after 100 cycles	100	88	This work
Mn_3O_4-1000 °C/40h	1174	415 after 100 cycles	100	67	This work

F-Mn_3O_4-1000 °C/40h by simple and easy route of heating	1686	783 after 100 cycles	100	77	This work

The rate performance of the F-doped and un-doped Mn_3O_4 materials are summarised in Fig. 8 (d). The coin cells were run at various current densities of 200, 500, 1000 and 2000 mA g^{-1} and directly swapped back to the initial current density of 200 mA g^{-1} in order to establish the stability of the cells after experiencing a series of high current densities. For all the cells, the reversible capacity decreases as the current density increases. Specific capacity of F-doped and un-doped Mn_3O_4 samples of the initial (1st cycle) and final (20th cycle) are listed in Table 4. As seen in Table 4, un-doped Mn_3O_4 samples exhibit moderately high capacity at initial cycles, but undergo severe capacity fading and low specific capacity at high current densities. The F-doped samples show the opposite results, wherein the specific capacities improve due to F-doping; at the current densities of 200, 500, 1000 and 2000 mA g^{-1}, the specific capacities are 1061, 604, 460, 131 and 649, 476, 347, 216 mAh g^{-1} for the F-doped Mn_3O_4- 850 °C/22h and Mn_3O_4-1000 °C/40h materials. After deep cycling at 2000 mA g^{-1}, the electrodes (F-doped Mn_3O_4-850 °C/22h and Mn_3O_4-1000 °C/40h) can recover the specific capacity of around 656 and 491 mAh g^{-1} when the current density was reduced back to 200 mA g^{-1}. At high current density (2000 mA g^{-1}), F-Mn_3O_4-1000 °C/40h shows a retrieved specific capacity of almost 1.65 times greater than that of F-Mn_3O_4-850 °C/22h sample. The capacity retention at 200 mA g^{-1} after examining at high current densities (200, 500, 1000 and 2000 mA g^{-1}) was 86 and 95% for F-Mn_3O_4-850 °C/22h and F-Mn_3O_4-1000 °C/40h, respectively. Nonetheless, F-Mn_3O_4-850 °C/22h exhibited highest capacity than the F-Mn_3O_4-1000 °C/40h. The fluorine doped Mn_3O_4 materials (850 °C/22h and 1000 °C/40h) showed highest capacity at all current densities, demonstrating the high power capability of the electrodes, which is higher than the other different structured Mn_3O_4 materials and its composites [10,18,19,22,24,28,48,49]. The improved rate capability of the F-doped cells is indicative of enhanced charge transportation possibly due to the dopant creating high defects for enhanced lithium-ion diffusion [41,50]. Also, our fluorination has been able to create nanoparticles to facilitate large accommodation of volume change during Li-ion insertion and extraction process.

Table 4 Rate capability data (discharge capacities) at different current densities ($1^{st}$and 20^{th}cycle) of 200, 500, 1000 and 2000 mA g^{-1} and the data observed from Fig. 8d.

alt-text: Table 4

Anode materials	Current density (mA g^{-1})									
	200		500		1000		2000		200	
	Capacity (mAh g^{-1})-cycles		Capacity (mAh g^{-1})-cycles		Capacity (mAh g^{-1})-cycles		Capacity (mAh g^{-1})-cycles		Capacity (mAh g^{-1}) - cycles	
	1^{st}	20^{th}	1^{st}	20^{th}	1^{st}	20^{th}	1^{st}	20^{th}	1^{st}	100^{th}
Mn_3O_4-850/22h	1358	806	680	408	318	108	49	18	869	499
F-Mn_3O_4-850/22h	1457	962	604	560	460	402	131	112	656	566
Mn_3O_4-1000/40h	1175	450	391	308	260	214	148	103	269	425
F-Mn_3O_4-1000/40h	1386	616	476	472	347	316	216	209	491	465

To understand the effect of fluorination on the kinetic properties of Li^+ ions of the anode materials (Mn_3O_4), the electrochemical impedance spectroscopy (EIS) experiments was ere carried out on the various coin cells before cycling (open circuit voltage, OCV≈ 2.6 V) and after cycling (100^{th} cycle, OCV). The Nyquist plots (Real vs. Imaginary) of all the materials (Fig. 9a-d) were fitted using an electrical equivalent circuit (Fig. 9e), details of which have been described elsewhere [51,52]. In the Nyquist plots, the dotted and the straight line represents the experimental and fitted data, respectively. The fresh cells of all the samples show a single depressed semicircle in the high frequency region, which is attributed to the combination of surface film and the charge transfer resistance ($R_{(sf+ct)}$) and constant phase elements ($CPE_{(sf+dl)}$). The R_{sf} arises due to the Li^+ ion passage through the solid-electrolyte interphase (SEI) film, and the R_{ct} is due to the electrode/electrolyte interface [53]. The constant-phase element ($CPE_{(sf+dl)}$) represents the surface film and double layer capacitance (C_{dl}), which is used instead of pure capacitor due to the inhomogeneous nature of the electrodes. The inclined slope in the low frequency region of the Nyquist plot is the Warburg-type behaviour of the electrodes which describes the resistance of the solid-state diffusion of Li^+ ions through the lattice and the intercalation capacitance of the compounds [54,55]. The values of the fitting EIS parameters are summarised in Table 5. The associated ($R_{(sf+ct)}$) and ($CPE_{(sf+dl)}$) values are 532,455,295,248 (±5Ω) and 32,21,31,31 (±3 μF) or pure and F-doped Mn_3O_4 (850 °C/22h and 1000 °C/40h), respectively. The α-values are in the range of 0.63–0.73, validating our choice for the CPE rather than the C_{dl}. The values of the electrolyte resistance (R_1) are 12, 10 and 12, 8 (±0.5Ω) for pure and F-doped Mn_3O_4 materials, respectively. Understandably, spectra observed after cycling (pure and doped Mn_3O_4) are qualitatively different from those obtained for fresh cells since the electrode process that has taken place in the composites. The second depressed semicircle is now well-developed in the mid-low frequency range, which clearly describes the bulk resistance (R_b) due to the electronic conductivity of the active material

and ionic conductivity of electrolyte in the pores of the composite electrodes. Also, the development of the R_b is made possible by the structural modification of the electrodes during cycling. The observed $R_{(sf+ct)}$ and R_b values~~-~~ after 100th cycle are so small ~~than fresh cell of~~ at 44, 8, 10 (±5Ω) and 56, 10, 16 (±3Ω) for pure Mn_3O_4-850 °C/22h and F-doped Mn_3O_4-850 °C/22h and Mn_3O_4-1000 °C/40h samples, respectively. On the other hand, the Mn_3O_4-1000 °C/40h exhibits only one semicircle after cycling and observed $R_{(sf+ct)}$ value is 90 (±5Ω).

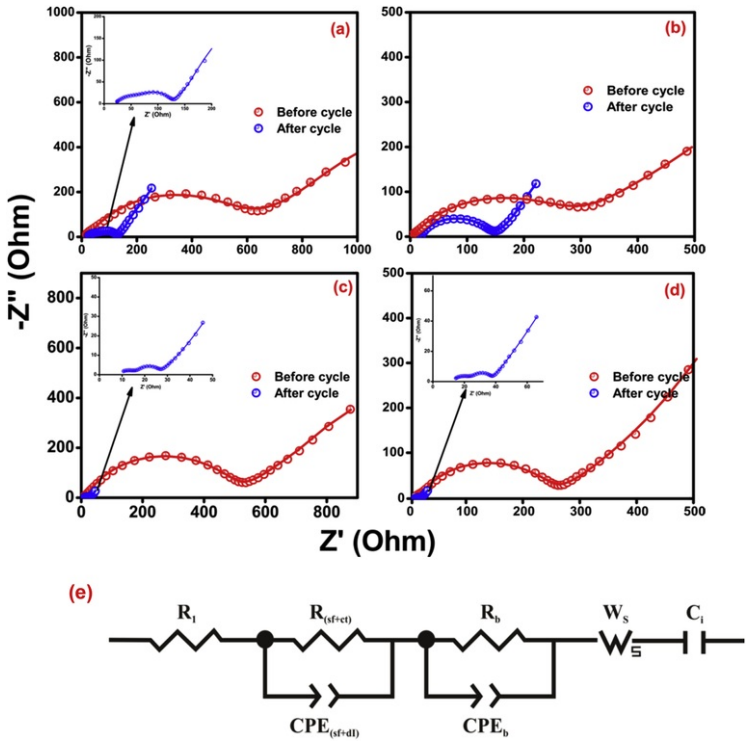

Fig. 9 Nyquist plots of pure (a) Mn_3O_4-850 °C/22h, (b)Mn_3O_4-1000 °C/40h and F-doped (c) F-Mn_3O_4-850 °C/22h, (d) F-Mn_3O_4-1000 °C/40h materials at fresh cell (OCV) and after aging cells (100^{th} cycles) and (e) displays the equivalent electrical circuit used fo fitting the elements of all the spectra.

alt-text: Fig. 9

Table 5 Fitted impedance parameters of pure and doped Mn3O4 materials by using the equivalent circuit.

alt-text: Table 5

Material	Aging cells	R_1 (±0.5Ω)	$R_{(sf+ct)}$ (±5Ω)	$CPE_{(sf+dl)}$ (±3 μF)	α (±0.02)	R_b (±3Ω)	$CPE_{(sf+ct)}$ (±3 μF)	W_s (±10Ω)	C_i (F)
Mn_3O_4-850 °C/22h	Fresh cells	12	532	32	0.69	–	–	1165	0.01
	100^{th} cycle	14	44	34	0.89	56	28	197	0.05
F-Mn_3O_4-850 °C/22h	Fresh cells	10	455	21	0.65	–	–	1186	–
	100^{th} cycle	7	8	32	0.71	10	26	92	0.21
Mn_3O_4-1000 °C/40h	Fresh cells	12	295	31	0.73	–	–	1085	–
	100^{th} cycle	20	90	30	0.88	–	–	131	0.05

F-Mn_3O_4-1000 °C/40h	Fresh cells	8	248	31	0.64	–	–	1369	–
	100th cycle	11	10	24	0.88	16	21	104	0.25

The relatively small electrolyte resistance (R_1) of 7 and 11Ω are found to be noticed for fluorine doped Mn_3O_4- 850 °C/22h and Mn_3O_4-1000 °C/40h, which is less than pure doped materials of 14 and 20Ω after cycling. The smallest surface resistance of F-doped materials might be due to the corrosion-resistant effect of fluorine, which protects the electrode surface from the undesirable attack of HF from the decomposition of the electrolyte. The intercalation capacitance (C_i) reflecting the occupation of the lithium-ion into the inserted site was found to be < 1 F at OCV and after cycling electrodes, which indicates that the absence of solid-state diffusion of Li ions into the anode matrix [2]. It is to be noted that, the observed low R_{ct} values of the doped compounds after cycling indicate the easy insertion and de-insertion of lithium ions during cycling, which is a further effect of F-doping. Consequently, high specific capacity should be obtained for F-doped Mn_3O_4 materials, which is good agreement with the rate capability performance test. In general, our EIS data provide critical insight into the charge-transfer properties of the anode materials as a result of the fluorination process. From the Nyquist plots of Fig. 9, it is observed that the fresh cells give higher impedance compared to the aged ones, which is indicative of the poor interfacial properties of the fresh cells. The improved interfacial properties of the aged cells may be related to the activation of the electrode materials by electrochemical cycling. Such activation may arise from structural re-organisation to allow for improved lithium-ion diffusivity within the crystalline lattice structure.

The enhanced electrochemical performance of the fluorinated Mn_3O_4 materials (in terms of cycling performance and lower impedance) could be associated with the successful surface fluorination of the materials. Some researchers [56–59] have made similar observation for lithium-ion battery layered cathode materials, but not for Mn_3O_4 anode materials. Hausmannite Mn_3O_4 has long been known as a tetragonally deformed spinel material due to the so-called Jahn-Teller (JT) effect [60]. JT effect is the leading cause of capacity fade in spinel electrode materials for lithium-ion batteries. Thus, the reason for the improved cycling stability for the F-Mn_3O_4 may be ascribed to the improved structural properties of the pristine Mn_3O_4 by the fluorination process. Partial fluorination is known to lead to the 'disappearance' of the Jahn-Teller effect [61]. Fluorination also decreases cell interfacial impedance, which benefits fast lithium-ion transfer kinetics. The integration of the fluorine-ion into Mn_3O_4 surface crystal lattice should assist in stabilizing the surface structure during electrochemical cycling process.

4 Conclusion

Hausmanite-Mn_3O_4 anode materials for application in lithium-ion batteries were directly synthesized from a low-cost EMD using facile two-step heat-treatment processes at different temperatures and times. The structure and the purity of the final products were confirmed with XRD and XPS data. Unlike the as-prepared anode materials, the F-doped counterparts showed enhanced capacity, cyclability and charge-transfer properties. Indeed, fluorination of EMD-derived Mn_3O_4 confer on the anode material an industrially-preferred spherical micro-structured/nanostructured morphology, promising an important synthetic route for the development of a simple and low-cost preparation of Mn_3O_4 with improved physico-electrochemical properties.

Acknowledgement

One of the authors NP is very grateful to Council for Scientific and Industrial Research (CSIR), Pretoria, South Africa for the financial support as post-doctoral fellow.

Appendix A. Supplementary data

Supplementary data related to this article can be found at https://doi.org/10.1016/j.matchemphys.2018.01.003.

References

[1] M.V. Reddy, G.V. Subba Rao and B.V.R. Chowdari, Metal oxides and oxysalts as anode materials for Li ion batteries, *Chem. Rev.* **113**, 2013, 5364–5457.

[2] S. Petnikota, V.V.S.S. Srikanth, P. Nithyadharseni, M.V. Reddy, S. Adams and B.V.R. Chowdari, Sustainable graphenothermal reduction chemistry to obtain MnO nanonetwork supported exfoliated graphene oxide composite and its electrochemical characteristics, *ACS Sustain. Chem. Eng.* **3**, 2015, 3205–3213.

[3] X. Pan, J. Ma, R. Yuan and X. Yang, Layered double hydroxides for preparing $CoMn_2O_4$ nanoparticles as anodes of lithium ion batteries, *Mater. Chem. Phys.* **194**, 2017, 137–141.

[4] P. Nithyadharseni, M.V. Reddy, H. Fanny, S. Adams and B.V.R. Chowdari, Facile one pot synthesis and Li-cycling properties of MnO_2, *RSC Adv.* **5**, 2015, 60552–60561.

[5] W. Chen, Z. Zhou, H. Liang, W. Ren and Z. Wang, Lithium copper/manganese titanate anode material for rechargeable lithium-ion batteries, *Mater. Chem. Phys.* **169**, 2016, 128–135.

[6] H. Gao, C.-L. Liu, Y. Liu, Z.-H. Liu and W.-S. Dong, MoO_2-loaded porous carbon hollow spheres as anode materials for lithium-ion batteries, *Mater. Chem. Phys.* **147**, 2014, 218–224.

[7] P. Nithyadharseni, M.V. Reddy, K.I. Ozoemena, F.I. Ezema, R.G. Balakrishna and B.V.R. Chowdari, Electrochemical performance of BaSnO3 anode material for lithium-ion battery prepared by molten salt method, *J. Electrochem. Soc.* **163**, 2016, A540–A545.

[8] Gang Wang, Ting Liu, Xiaoling Xie, Zhaoyu Ren and Hui Wang, Structure and electrochemical performance of Fe_3O_4/graphene nanocomposite as anode material for lithium-ion batteries, *Mater. Chem. Phys.* **128**, 2011, 336–340.

[9] P. Nithyadharseni, M.V. Reddy, B. Nalini, T.R. Ravindran, B.C. Pillai, M. Kalpana and B.V.R. Chowdari, Electrochemical studies of CNT/Si-SnSb nanoparticles for lithium ion batteries, *Mater. Res. Bull.* **70**, 2015, 478–485.

[10] C. Wang, L. Yin, D. Xiang and Y. Qi, Uniform carbon layer coated Mn_3O_4 nanorod anodes with improved reversible capacity and cyclic stability for lithium ion batteries, *ACS Appl. Mater. Interfaces* **4**, 2012, 1636–1642.

[11] Q. Li, L. Yin, Z. Li, X. Wang, Y. Qi and J. Ma, Copper doped hollow structured manganese oxide mesocrystals with controlled phase structure and morphology as anode materials for lithium ion battery with improved electrochemical performance, *ACS Appl. Mater. Interfaces* **5**, 2013, 10975–10984.

[12] D. Pasero, N. Reeves and A.R. West, Co-doped Mn_3O_4: a possible anode material for lithium batteries, *J. Power Sources* **141**, 2005, 156–158.

[13] S.K. Srivastava, B. Kartick, S. Choudhury and M. Stamm, Thermally fabricated MoS_2-graphene hybrids as high performance anode in lithium ion battery, *Mater. Chem. Phys.* **183**, 2016, 383–391.

[14] Y. Deng, L. Wan, Y. Xie, X. Qin and G. Chen, Recent advances in Mn-based oxides as anode materials for lithium ion batteries, *RSC Adv.* **4**, 2014, 23914–23935.

[15] J. Gao, M.A. Lowe and H.c.D. Abruna, Spongelike nanosized Mn_3O_4 as a high-capacity anode material for rechargeable lithium batteries, *Chem. Mater.* **23**, 2011, 3223–3227.

[16] J. Wang, N. Du, H. Wu, H. Zhang, J. Yu and D. Yang, Order-aligned Mn_3O_4 nanostructures as super high-rate electrodes for rechargeable lithium-ion batteries, *J. Power Sources* **222**, 2013, 32–37.

[17] C. Wang, L. Yin, D. Xiang and Y. Qi, Uniform carbon layer coated Mn_3O_4 nanorod anodes with improved reversible capacity and cyclic stability for lithium ion batteries, *ACS Appl. Mater. Interfaces* **4**, 2012, 1636–1642.

[18] N. Wang, J. Yue, L. Chen, Y. Qian and J. Yang, Hydrogenated TiO_2 branches coated Mn_3O_4 nanorods as an advanced anode material for lithium ion batteries, *ACS Appl. Mater. Interfaces* **7**, 2015, 10348–10355.

[19] S.-K. Park, A. Jin, S.-H. Yu, J. Ha, B. Jang, S. Bong, S. Woo, Y.-E. Sung and Y. Piao, Situ hydrothermal synthesis of Mn_3O_4 nanoparticles on nitrogen-doped graphene as high-performance anode materials for lithium ion batteries, *Electrochim. Acta* **120**, 2014, 452–459.

[20] M. Eastman, A. Besser, Y. Chen and J. Jiao, Hydrothermal synthesis of core/shell ZnO: Mn/Mn3O4 nanowires, *J. Phys. Chem. C* **115**, 2011, 10979–10984.

[21] Z. Bai, N. Fan, Z. Ju, C. Guo, Y. Qian, B. Tang and S. Xiong, Facile synthesis of mesoporous Mn_3O_4 nanotubes and their excellent performance for lithium-ion batteries, *J. Mater. Chem.* **1**, 2013, 10985–10990.

[22] D. Zhao, Q. Hao and C. Xu, Facile fabrication of composited Mn_3O_4/Fe_3O_4 nanoflowers with high electrochemical performance as anode material for lithium ion batteries, *Electrochim. Acta* **180**, 2015, 493–500.

[23] J. Yue, X. Gu, L. Chen, N. Wang, X. Jiang, H. Xu, J. Yang and Y. Qian, General synthesis of hollow MnO_2, Mn_3O_4 and MnO nanospheres as superior anode materials for lithium ion batteries, *J. Mater. Chem.* **2**, 2014, 17421–17426.

[24] G. Jian, Y. Xu, L.-C. Lai, C. Wang and M.R. Zachariah, Mn_3O_4 hollow spheres for lithium-ion batteries with high rate and capacity, *J. Mater. Chem.* **2**, 2014, 4627–4632.

[25] X. Gu, J. Yue, L. Li, H. Xue, J. Yang and X. Zhao, General synthesis of MnO_x (MnO_2, Mn_2O_3, Mn_3O_4, MnO) hierarchical microspheres as lithium-ion battery anodes, *Electrochim. Acta* **184**, 2015, 250–256.

[26] Z.H. Wang, l. x. Yuan, Q.G. Shao, F. Huang and Y.H. Huang, Mn_3O_4 nanocrsytals anchored on multi-walled carbon nanotube as high-performance anode materials for lithium-ion batteries, *Mater. Lett.* **80**, 2012, 110–113.

[27] S.-Z. Huang, J. Jin, Y. Cai, Y. Li, H.-Y. Tan, H.-E. Wang, G. Van Tendeloo and B.-L. Su, Engineering single crystalline Mn_3O_4 nano-octahedra with exposed highly active {011} facets for high performance lithium ion batteries, *Nano* **6**, 2014, 6819–6827.

[28] Y. Wang, Coprecipitated 3D nanostructured graphene oxide/Mn_3O_4 hybrid as anode of lithium-ion batteries, *J. Mater. Res.* **30**, 2015, 484–492.

[29] Y. Liu, W. Wang, Y. Wang, Y. Ying, L. Sun and X. Peng, Binder-free three-dimensional porous Mn_3O_4 nanorods/reduced graphene oxide paper-like electrodes for electrochemical energy storage, *RSC Adv.* **4**, 2014, 16374–16379.

[30] L. Li, Z. Guo, A. Du and H. Liu, Rapid microwave-assisted synthesis of Mn_3O_4-graphene nanocomposite and its lithium stroage properties, *J. Mater. Chem.* **22**, 2012, 3600–3605.

[31] H. Wang, L.-F. Cui, Y. Yang, H. Sanchez Casalongue, J.T. Robinson, Y. Liang, Y. Cui and H. Dai, Mn_3O_4/Graphene hybrid as a high-capacity anode material for lithium ion batteries, *J. Am. Chem. Soc.* **132**, 2010, 13978–13980.

[32] Y.R. Ren, J.W. Wang, X. Huang, B. Yang and J. Ding, One step hydrothermal synthesis of Mn_3O_4/graphene composites with great electrochemical properties for lithium-ion batteries, *RSC Adv.* **7**, 2015, 59208–59217.

[33] J.-G. Wang, D. Jin, R. Zhou, X. Li, X.-r. Liu, C. Shen, K. Xie, B. Li, F. Kang and B. Wei, Highly flexible Graphene/Mn_3O_4 nanocomposite membrane as advanced anodes for Li-Ion batteries, *ACS Nano* **10**, 2016, 6227–6234.

[34] H. Tao, Z. Feng, H. Liu, X. Kan and P. Chen, Reality and future of rechargeable lithium batteries, *Open Mater. Sci. J.* **5**, 2011, 204–214.

[35] L. Ji, A.J. Medford and X. Zhang, Porous carbon nanofibers loaded with manganese oxide particles: formation mechanism and electrochemical performance as energy-storage materials, *J. Mater. Chem.* **19**, 2009, 5593–5601.

[36] F. Ma, A. Yuan and J. Xu, Nanoparticulate Mn_3O_4/VGCF composite conversion-anode material with extraordinarily high capacity and excellent rate capability for lithium ion batteries, *ACS Appl. Mater. Interfaces* **6**, 2014, 18129–18138.

[37] M. Nagao, A. Hayashi and M. Tatsumisago, Sulfur–carbon composite electrode for all-solid-state Li/S battery with Li2S–P2S5 solid electrolyte, *Electrochim. Acta* **56**, 2011, 6055–6059.

[38] Y. Ma, C. Fang, B. Ding, G. Ji and J.Y. Lee, Fe-doped MnxOy with hierarchical porosity as a high-performance lithium-ion battery anode, *Adv. Mater.* **25**, 2013, 4646–4652.

[39] R. Jin, H. Liu, Y. Guan, J. Zhou and G. Li, Molten salt synthesis of fluorine-doped Mn_3O_4 nanobelts as anode materiasl for Li-ion batteries, *CrystEngComm* **17**, 2015, 7717–7722.

[40] Y. Ma, B. Ding, G. Ji and J.Y. Lee, Carbon-Encapsulated F-doped $Li_4Ti_5O_{12}$ as a high rate anode materiasl for Li^+ batteries, *ACS Nano* **7**, 2013, 10870–10878.

[41] J. Sun, L. Xiao, S. Jiang, G. Li, Y. Huang and J. Geng, Fluorine-doped SnO2@ graphene porous composite for high capacity lithium-ion batteries, *Chem. Mater.* **27**, 2015, 4594–4603.

[42] R. Kumar, P.N. Funeka, V. Elumalai, K.M. Mkhulu, D. Krishnan and I.O. Kenneth, Microwave-enhanced electrochemical cycling performance of the $LiNi_{0.2}Mn_{1.8}O_4$ spinel cathode material at elevated temperature, *Phys. Chem. Chem. Phys.* **18**, 2016, 13074–13083.

[43] X. Fang, X. Lu, X. Guo, Y. Mao, Y.-S. Hu, J. Wang, Z. Wang, F. Wu, H. Liu and L. Chen, Electrode reactions of manganese oxides for secondary lithium batteries, *Elec. Chem. Comm* **12**, 2010, 1520–1523.

[44] F.P. Nkosi, K. Raju, P. Nithyadharseni, M.V. Reddy, C. Billing and K.I. Ozoemena, Insights into the synergitic roles of microwave and fluorination treatments towards enhamncing the cycling stability of P2-type $Na_{0.67}[Mg_{0.28}Mn_{0.72}]O_2$ cathode materials for sodium-ion batteries, *J. Electrochem. Soc.* **164**, 2017, A3362–A3370.

[45] Y. Xiao, D.-E. Wittmer, F. Izumi, S. Mini, T. Graber and P.-J. Viccaro, Determination of cations distribution in Mn_3O_4 by anomalous X-ray powder diffraction, *Appl. Phys. Lett.* **85**, 2004, 736.

[46] M. Jing, H. Hou, Y. Yang, Y. Zhang, X. Yang, Q. Chen and X. Ji, Electrochemically alternating voltgae induced Mn_3O_4/Graphite composite with enhanced electrochemical performances for lithium-ion batteries, *Electrochim. Acta* **155**, 2015, 157–163.

[47] H. Zhang, G. Cao, Z. Wang, Y. Yang, Z. Shi and Z. Gu, Growth of manganese oxide nanoflowers on vertically-aligned carbon nanotube arrays for high-rate electrochemical capacitive energy storage, *Nano Lett.* **8**, 2008 2664–2668.

[48] I.A. Ayhan, Q. Li, P. Meduri, H. Oh, G.R. Bhimanapati, G. Yang, J.A. Robinson and Q. Wang, Effect of Mn_3O_4 nanoparticle composition and distribution on graphene as a potential hybrid anode material for lithium-ion batteries, *RSC Adv.* **6**, 2002, 33022–33030.

[49] I. Nam, N.D. Kim, G.-P. Kim, J. Park and J. Yi, One step preparation of Mn_3O_4/graphene composites for use as an anode in Li ion batteries, *J. Power Sources* **244**, 2013, 56–62.

[50] H.-W. Ha, K. Kim, M.d. Borniol and T. Toupance, Fluorine-doped nanocrystalline SnO_2 powders prepared via a single molecular precursor method as anode materials for Li-ion batteries, *J. Solid State Chem.* **179**, 2006, 702–707.

[51] P. Nithyadharseni, M.V. Reddy, K.I. Ozoemena, R.G. Balakrishna and B.V.R. Chowdari, Low temperature molten salt synthesis of $Y_2Sn_2O_7$ anode material for lithium ion batteries, *Electrochim. Acta* **182**, 2015, 1060–1069.

[52] P. Nithyadharseni, M.V. Reddy, B. Nalini, M. Kalpana and B.V.R. Chowdari, Sn-based intermetallic alloy anode materials for the application of lithium ion batteries, *Electrochim. Acta* **161**, 2015, 261–268.

[53] M.V. Reddy, G.V. Subba Rao and B.V.R. Chowdari, Nano-$(V_{1/2}Sb_{1/2}Sn)O_4$: a high capacity, high rate anode material for Li-ion batteries, *J. Mater. Chem.* **21**, 2011, 10003–10011.

[54] A. Sakunthala, M.V. Reddy, S. Selvasekarapandian, B.V.R. Chowdari and P. Christopher Selvin, Energy storage studied of bare and doped vanadium pentoxide, $(V_{1.95}M_{0.05})O_5$, M=Nb, Ta, for lithium ion battreies, *Energy Environ. Sci.* **4**, 2011, 1712–1725.

[55] P. Nithyadharseni, M.V. Reddy, B. Nalini, P. Saravanan, V.T.P. Vinod, M. Cernik and B.V.R. Chowdari, Spark plasma-sintered Sn-based intermetallic Alloys and their Li-stroage studies, *J. Solid State Electrochem.* **20**, 2016, 1743–1751.

[56] H. Zhang and T. Song, Synthesis and performance of fluorine substituted $Li_{1.05}(Ni_{0.5}Mn_{0.5})_{0.95}O_{2-x}F_x$ cathode materials modified by surface coating with $FePO_4$, *Electrochim. Acta* **114**, 2013, 116–124.

[57] S.H. Kang and K. Amine, Layered $Li(Li_{0.2}Ni_{0.15+0.5z}Co_{0.10}Mn_{0.55-0.5z})O_{2-z}F_z$ cathode materials for Li-ion secondary batteries, *J. Power Sources* **146**, 2005, 654–657.

[58] H. Li and L.Z. Fan, Effects of fluorine substitution on the electrochemical performance of layered Li-excess nickel manganese oxides cathode materials for lithium-ion batteries, *Electrochim. Acta* **113**, 2013, 407–411

[59] Y. Wu and A. Manthiram, Effect of Al^{3+} and F^- doping on the irreversible oxygen loss from layered $Li[Li_{0.17}Mn_{0.58}Ni_{0.25}]O_2$ cathodes, *Electrochem. Solid State Lett.* **10**, 2007, A151–A154.

[60] D. Jarosch, Crystal structure refinement and reflectance measurements of hausmannite, Mn_3O_4, *Mineral. Petrol.* **37**, 1987, 15–23.

[61] ~~H. Koppel, D.R. Yarkony and H. Barentzen, The John-Teller Effect-Fundamentals and implications for physics and chemistry, 2010, Spinger.~~ (Please REPLACE as follows: Faraji S., Gindensperger E., Köppel H. (2009) Multi-Mode Jahn–Teller and Pseudo-Jahn–Teller Effects in Benzenoid Cations. In: Köppel H., Yarkony D., Barentzen H. (eds) The Jahn-Teller Effect. Springer Series in Chemical Physics, vol 97, pp239-276. Springer, Berlin, Heidelberg)

Appendix A. Supplementary data

The following is the supplementary data related to this article:

Multimedia Component 1

Supplementary material

alt-text: Supplementary material

Highlights

- Fluorinated-Mn_3O_4 nanospheres have been prepared from electrolytic manganese dioxide (EMD).
- Innovatively, fluorination process is able to tune the general physico-chemistry of Mn_3O_4.
- Fluorination process leads to enhanced capacity, rate capability, cyclability and charge-transport properties.
- F-Mn_3O_4 serves as a low-cost, high-performing anode material for lithium-ion batteries.

Queries and Answers

Query: Please check the designated corresponding author is correct, and amend if necessary.
Answer: All correct.

Query: Please note that author's telephone/fax numbers are not published in Journal articles due to the fact that articles are available online and in print for many years, whereas telephone/fax numbers are changeable and therefore not reliable in the long term.

Answer: I accept.

Query: Please provide the volume number or issue number or page range or article number for the bibliography in Ref(s). [61].
Answer: Faraji S., Gindensperger E., Köppel H. (2009) Multi-Mode Jahn–Teller and Pseudo-Jahn–Teller Effects in Benzenoid Cations. In: Köppel H., Yarkony D., Barentzen H. (eds) The Jahn-Teller Effect. Springer Series in Chemical Physics, vol 97, pp 239-276. Springer, Berlin, Heidelberg

Query: Please confirm that given names and surnames have been identified correctly and are presented in the desired order and please carefully verify the spelling of all authors' names.
Answer: Yes

Query: Your article is registered as a regular item and is being processed for inclusion in a regular issue of the journal. If this is NOT correct and your article belongs to a Special Issue/Collection please contact s.shanmugam@elsevier.com immediately prior to returning your corrections.
Answer: Yes